A New Finite-Volume Approach to Efficient Discretization on Challenging Grids

I. Aavatsmark, G.T. Eigestad, and **B.-O. Heimsund,** Center for Integrated Petroleum Research; **B.T. Mallison,** Chevron; **J.M. Nordbotten,** University of Bergen; and **E. Øian,** Center for Integrated Petroleum Research

Summary

Multipoint-flux-approximation (MPFA) methods were introduced to solve control-volume formulations on general simulation grids for porous-media flow. While these methods are general in the sense that they may be applied to any matching grid, their convergence properties vary.

An important property for multiphase flow is the monotonicity of the numerical elliptic operator. In a recent paper (Nordbotten et al. 2007), conditions for monotonicity on quadrilateral grids have been developed. These conditions indicate that MPFA formulations that lead to smaller flux stencils are desirable for grids with high aspect ratios or severe skewness and for media with strong anisotropy or strong heterogeneity. The ideas were pursued recently in Aavatsmark et al. (2008), where the L-method was introduced for general media in 2D. For homogeneous media and uniform grids, this method has four-point flux stencils and seven-point cell stencils in two dimensions. The reduced stencils appear as a consequence of adapting the method to the closest neighboring cells.

Here, we extend the ideas for discretization on 3D grids, and ideas and results are shown for both conforming and nonconforming grids. The ideas are particularly desirable for simulation grids that contain faults and local grid refinement.

We present numerical results herein that include convergence results for single-phase flow on challenging grids in 2D and 3D and for some simple two-phase results. Also, we compare the L-method with the O-method.

Introduction

In reservoir simulation, control-volume formulations with two-point flux approximations (TPFAs) are used generally to approximate the elliptic operator:

$$Lu = -\mathrm{div}\left(\mathbf{K}\ \mathrm{grad}\ u\right), \dots\dots\dots\dots\dots\dots\dots\dots\dots\dots\dots (1)$$

which we here consider in both two and three dimensions. The tensor $\mathbf{K}$ is the permeability, and it is assumed to be symmetric and positive definite. The potential u is the pressure. TPFAs are physically intuitive, and the discretization of the operator (Eq. 1) results in an M-matrix. However, for non-$\mathbf{K}$-orthogonal grids, TPFA gives an error in the solution that does not vanish as the grids are refined (Aavatsmark 2007; Wu and Parashkevov 2009).

To be able to solve the flow equations on general grids, MPFA methods have been suggested. The most popular method has been the O-method, which, for quadrilaterals, is discussed in Aavatsmark (2002), Aavatsmark et al. (1996, 1998, 2006a), Edwards (2002), and Edwards and Rogers (1998). In this method, the transmissibility coefficients are calculated by requiring continuity of potential and flux at the interfaces of the cells in an interaction region. The potential is required only to be continuous at a point on each interface, and different locations of the continuity point yield different methods. This general formulation of the method was introduced by Edwards and Rogers (1998; Edwards 2002). In this paper, we apply only the special case of the   method in which the continuity point lies at the midpoint of the interfaces. This is

the classical O-method (Aavatsmark 2002; Aavatsmark et al. 1996, 1998, 2006a), which reduces to TPFA for $\mathbf{K}$-orthogonal grids. It is symmetric for general parallelepiped grids on heterogeneous media.

Convergence proofs of the 2D O-method are given in Aavatsmark et al. (2007), Klausen and Winther (2006a, 2006b), and Wheeler and Yotov (2006a, 2006b). Convergence rates have also been tested numerically; see Aavatsmark et al. (2006a, 2007), Edwards and Rogers (1998), Eigestad and Klausen (2005), Aavatsmark and Eigestad (2006), and Pal et al. (2006). Edwards and Rogers (1998) and Pal et al. (2006) compare convergence for general location of the continuity point. When the O-method is used for quadrilaterals that are not parallelograms, the quadrilaterals have to satisfy a condition to ensure convergence. A condition that is sufficient for convergence of potential and flux was given in Klausen and Winther (2006b). When this condition is exceeded, the rate of convergence is reduced and ultimately—for large excesses—convergence is lost. The same behavior can be observed for other nonsymmetric MPFA methods.

When an MPFA method is applied for multiphase flow, a monotone scheme for the operator (Eq. 1) is desirable. With monotone schemes, a discrete version of the maximum principle is fulfilled (Nordbotten et al. 2007). The discrete maximum principle is defined analogous to the maximum principle for differential equations. Therefore, it is expected that spurious oscillations and spurious extrema on no-flow boundaries do not occur for monotone schemes. M-matrix properties are discussed in Edwards and Rogers (1998) and Edwards and Zheng (2008), while general maximum principles for the MPFA methods are discussed in Nordbotten et al. (2007) and Nordbotten and Aavatsmark (2005). Local criteria that ensure monotonicity for general control-volume nine-point methods on heterogeneous media are given in Nordbotten et al. (2007). In Keilegavlen et al. (2009), it is shown that most of these criteria are also necessary for monotonicity. When these criteria are exceeded, undesirable oscillations or undesirable extrema on no-flow boundaries may occur for the potential. However, because the methods are exact for linear potential fields, such undesirable effects are observed only for truly nonlinear solutions (e.g., near wells).

Because the O-method is conditionally convergent and monotone, it is natural to ask if there are other MPFA methods with a larger domain of convergence and monotonicity. In this paper, we discuss a method, which we call the L-method, that uses fewer control volumes to calculate transmissibility coefficients. The method was first suggested in 2D in Aavatsmark et al. (2006b, 2008) and was initially motivated by optimal monotonicity criteria derived in Nordbotten et al. (2007). The ideas of the L-method discretization build on a careful selection of interacting cells that should approximate fluxes for subinterfaces of control volumes in a local region. To derive transmissibilities for the L-method, the principle of flux continuity is used together with full potential continuity across cell interfaces. These ideas will also be applicable for grids containing local grid refinement, making the method very flexible.

In this paper, the L-method is extended to 3D. In 2D, the L-method was shown to lead to a seven-point cell stencil for uniform parallelogram grids on homogeneous media; see Aavatsmark et al. (2008). In 3D, the L-method will be shown to lead to a 13-point cell stencil for uniform parallelepipeds on homogeneous media. This is in contrast to the 27-point stencil that is obtained for the O-method for the same case.
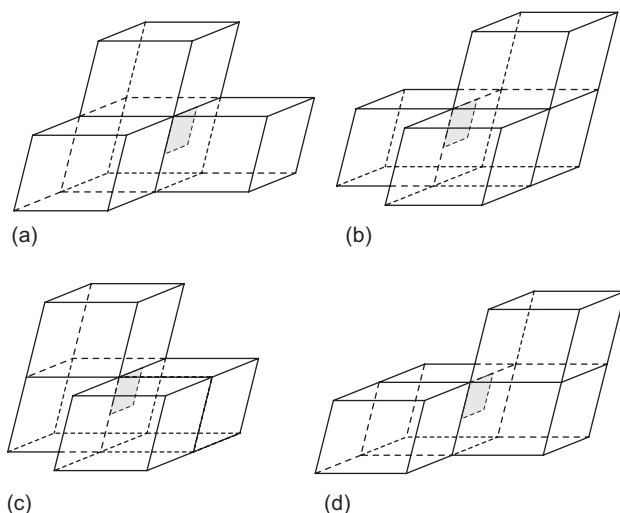
Fig. 1—The four L-stencils of the lower-back subinterface in an interaction volume; (a) A, (b) B, (c) C, and (d) D.

Fig. 2—Cell and point numbering in an L-stencil.

For general grids and media, the number of points in the cell stencil lies between 13 and 19. The selection of points works well for the cases that we have tested; however, for more-challenging cases, some generalizations or extensions may be required. For general grids, there is no guarantee that the method captures the principal grid direction in an optimal way.

We discuss the L-method and compare it with the O-method in 3D. These results may be compared with the results of the recent papers (Edwards and Zheng 2008; Pal and Edwards 2007; Chen et al. 2008), in which closely related but quite distinct alternatives to the L-method are introduced.

A useful feature of the L-method is its flexibility for general grids. Because the method conveniently selects three interacting cells in 2D and four interacting cells in 3D, the method comes as a natural candidate for discretization on simulation grids containing faults and local grid refinement (LGR) (Øian et al. 2006).

L-Method in 3D

Details of the L-method in 2D may be found in Aavatsmark et al. (2006b, 2008), together with extensive numerical single-phase tests.
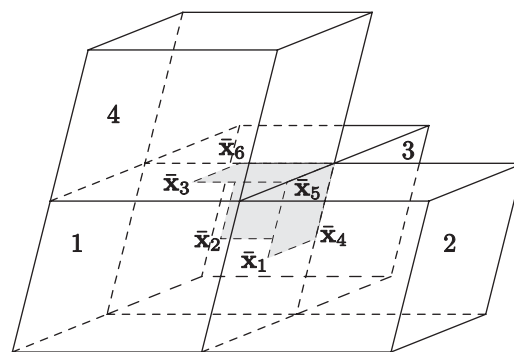
In 3D, the L-method becomes a convenient tool for constructing flux molecules on very general grids. This is particularly useful when faults or LGRs are used in the simulation grids. MPFA ideas have been considered previously for faults in Aavatsmark et al. (2001a, 2001b), where special flux molecules were constructed on the basis of the number of cells that met at corners of grid cells. Numerical results showed significant improvement over standard TPFA discretization for nonmatching grids at the cost of rather complex flux molecules. The L-method ideas for such grids will result in simpler discretization than the special flux molecules pursued in Øian et al. (2006) and Aavatsmark et al. (2001b), and fluxes will always be given from a local system that conveniently uses information from four interacting cells. The interacting cells will be chosen by simple rules explained later.

First, we shall consider the method on conforming meshes in 3D and make some comparative studies with the standard O-method for single-phase flow. Analogously to 2D, we discuss the parallelepiped case on homogeneous media in detail.

The L-method will be pursued further for complex simulation grids containing faults and LGRs.

Framework for L-Method Implementation in 3D

We now consider the L-method framework for general 3D cases. First, we discuss transmissibility calculations for structured hexahedral grids. As for the O-method, the transmissibility coefficients are calculated for each subinterface, each subinterface consisting of a quarter of an interface between two cells. To compute the trans-missibility coefficients of a subinterface, four possible L-stencils are considered. **Fig. 1** shows the four L-stencils of the lower-back subinterface in an interaction volume. Each L-stencil contains four cells. Two of these four cells are the two cells sharing the subinterface. They are termed the central cells. The other two cells of an L-stencil have a corner at the subinterface and share a surface with one or both of the central cells but not with each other. For each subinterface, we compute the transmissibility coefficients for each of the four L-stencils. Then, we compare the transmissibility coefficients of the central cells, thus picking only one L-stencil for each subinterface. That is discussed later.

We now discuss the computation of the transmissibility coefficients of an L-stencil. It consists of four cells, and linear potentials in each subcell are assumed. To form a solvable local system, flux continuity together with full potential continuity across the subinterfaces is needed. In total, four degrees of freedom are available for each subcell when the potential is assumed to vary linearly, so that 16 degrees of freedom are available in total. One flux constraint and three potential constraints for each of the three subinterfaces yield 12 constraints altogether, and when the four node potentials are honored, we arrive at the desired 16 constraints. Note, however, that a large system need never be constructed. Because of the underlying sparsity, we need to invert only a 3×3 matrix to solve the local system. The resulting transmissibility matrix will operate only on the four node pressures.

It is convenient to divide the discussion of the transmissibility calculation into two parts. The two upper L-stencils in Fig. 1 are termed "centered" L-stencils, while the two lower L-stencils in Fig. 1 are termed "noncentered" L-stencils.

We first discuss transmissibility calculation in centered L-stencils. Such an L-stencil is shown in **Fig. 2.** With this L-stencil, transmissibility coefficients of the three subinterfaces (shown as gray surfaces) may be calculated. The potential is assumed to vary linearly for each grid cell. As will be shown, the local system of flux continuity may be expressed in terms of the four node potentials of the interacting cells, together with the potentials at the three interface midpoints, denoted $\bar{\mathbf{x}}_1$, $\bar{\mathbf{x}}_2$, and $\bar{\mathbf{x}}_3$ in Fig. 2. Some or all of the transmissibilities may be used to assemble the flux stencils of the entire interfaces.

Cell 1 in Fig. 2 in some ways will be dominant for the degrees of freedom of the local system that determines the subinterface fluxes. The gradient in Cell 1 is determined from the equations

$$\nabla U_1 \cdot \left(\bar{\mathbf{x}}_j - \mathbf{x}_1 \right) = \bar{u}_j - u_1, \quad j = 1,2,3, \dots\dots\dots\dots\dots (2)$$

where $\bar{u}_j$ and u_j are the potentials at $\bar{\mathbf{x}}_j$ and $\mathbf{x}_j$, respectively. The matrix of coefficients of the gradient in Eq. 2 and its inverse are given by

$$\mathbf{X} = \begin{bmatrix} \left(\bar{\mathbf{x}}_1 - \mathbf{x}_1 \right)^{\mathrm{T}} \\ \left(\bar{\mathbf{x}}_2 - \mathbf{x}_1 \right)^{\mathrm{T}} \\ \left(\bar{\mathbf{x}}_3 - \mathbf{x}_1 \right)^{\mathrm{T}} \end{bmatrix}, \quad \mathbf{X}^{-1} = \frac{1}{T_1} \left[\nu_{11}, \nu_{12}, \nu_{13} \right]. \dots\dots\dots\dots (3)$$

Here, the vectors ν_{1k}, $k = 1,2,3$ are

$$\nu_{1k} = \left(\bar{\mathbf{x}}_l - \mathbf{x}_1\right) \times \left(\bar{\mathbf{x}}_m - \mathbf{x}_1\right), \dots \dots \dots \dots \dots \dots (4)$$

where the indices $k,l,m \in \{1,2,3\}$ are cyclic. The determinant T_1 is the triple product,

$$T_1 = \left(\left(\bar{\mathbf{x}}_1 - \mathbf{x}_1\right)\left(\bar{\mathbf{x}}_2 - \mathbf{x}_1\right)\left(\bar{\mathbf{x}}_3 - \mathbf{x}_1\right)\right). \dots \dots \dots \dots (5)$$

The vectors ν_{1k} are inward normal vectors of a variational tetrahedron in Cell 1, and T_1 is six times the volume of this tetrahedron; see Aavatsmark (2002) for details. It follows that the gradient in Cell 1 can be expressed as

$$\nabla U_1 = \frac{1}{T_1} \sum_{k=1}^{3} \nu_{1k}\left(\bar{u}_k - u_1\right). \dots \dots \dots \dots \dots \dots (6)$$

The gradient in the other three cells can be expressed similarly. We introduce pressures at the additional points $\bar{\mathbf{x}}_4$, $\bar{\mathbf{x}}_5$, and $\bar{\mathbf{x}}_6$, depicted in Fig. 2, and term these $\bar{u}_4$, $\bar{u}_5$, and $\bar{u}_6$. Then, the potential of Cell 2, for example, may be spanned by the potential at the points $\bar{\mathbf{x}}_1$, $\bar{\mathbf{x}}_4$, and $\bar{\mathbf{x}}_5$ and the node $\mathbf{x}_2$.

The linear pressure variation of Cell 1 is used to express the potentials $\bar{u}_4$, $\bar{u}_5$, and $\bar{u}_6$,

$$\bar{u}_{3+j} = \nabla U_1 \cdot \left(\bar{\mathbf{x}}_{3+j} - \mathbf{x}_1\right) + u_1, \quad j = 1,2,3. \dots \dots \dots \dots (7)$$

Now, we introduce the vectors

$$\mathbf{r}_j = \left(\bar{\mathbf{x}}_{3+j} - \mathbf{x}_1\right), \quad j = 1,2,3 \dots \dots \dots \dots \dots \dots (8)$$

and the fractions

$$r_{1ij} = \nu_{1i}^{\mathrm{T}} \mathbf{r}_j / T_1, \quad i,j = 1,2,3. \dots \dots \dots \dots \dots \dots (9)$$

The index $i = 1, 2, 3$ denotes the flux interface number. We may now express potentials of the points $\bar{\mathbf{x}}_4$, $\bar{\mathbf{x}}_5$, and $\bar{\mathbf{x}}_6$ by the potential variation of Cell 1,

$$\bar{u}_4 = r_{111}\left(\bar{u}_1 - u_1\right) + r_{121}\left(\bar{u}_2 - u_1\right) + r_{131}\left(\bar{u}_3 - u_1\right),$$
$$\bar{u}_5 = r_{112}\left(\bar{u}_1 - u_1\right) + r_{122}\left(\bar{u}_2 - u_1\right) + r_{132}\left(\bar{u}_3 - u_1\right),$$
$$\bar{u}_6 = r_{113}\left(\bar{u}_1 - u_1\right) + r_{123}\left(\bar{u}_2 - u_1\right) + r_{133}\left(\bar{u}_3 - u_1\right). \dots \dots \dots \dots (10)$$

For the flux continuity of interface i, we use the normal vector $\mathbf{n}_i$, which has length equal to the area of the flux interface. For nonplanar surfaces, this vector is given by Eq. 26 in Aavatsmark and Eigestad (2006). The flux-continuity equation for local Subinterface 1 in the L-stencil in Fig. 2 then reads

$$-\mathbf{n}_1^{\mathrm{T}} \mathbf{K}_1 \nabla U_1 = -\mathbf{n}_1^{\mathrm{T}} \mathbf{K}_2 \nabla U_2, \dots \dots \dots \dots \dots \dots (11)$$

where $\mathbf{K}_j$ is the permeability and ∇U_j is the gradient in cell j. Using Eq. 6, Eq. 11 becomes

$$\frac{\mathbf{n}_1^{\mathrm{T}} \mathbf{K}_1}{T_1}\left[\sum_{k=1}^{3} \nu_{1k}\left(\bar{u}_{1k} - u_1\right)\right] = \frac{\mathbf{n}_1^{\mathrm{T}} \mathbf{K}_2}{T_2}\left[\sum_{k=1}^{3} \nu_{2k}\left(\bar{u}_{2k} - u_2\right)\right]. \dots \dots (12)$$

The double indexing of the interface-point potentials refers to the local numbering k of the points as seen from Cells 1 and 2, respectively. In particular, we have that

$$\bar{u}_{11} = \bar{u}_1,$$
$$\bar{u}_{12} = \bar{u}_2,$$
$$\text{and } \bar{u}_{13} = \bar{u}_3, \dots \dots \dots \dots \dots \dots (13)$$

and

$$\bar{u}_{21} = \bar{u}_4,$$
$$\bar{u}_{22} = \bar{u}_1,$$
$$\text{and } \bar{u}_{23} = \bar{u}_5. \dots \dots \dots \dots \dots \dots \dots (14)$$

Inserting the pressure expressions (Eq. 10) for $\bar{u}_4$ and $\bar{u}_5$, the flux-continuity condition is expressed in terms of the four node pressures u_1, u_2, u_3, and u_4 and the three interface midpoint pressures $\bar{u}_1$, $\bar{u}_2$, and $\bar{u}_3$. In Eq. 14, the coefficients are expressed by the fractions of Eq. 9 and the fractions

$$\omega_{ijk} = \frac{\mathbf{n}_i^{\mathrm{T}} \mathbf{K}_j \nu_{jk}}{T_j}. \dots \dots \dots \dots \dots \dots (15)$$

Similar equations follow from flux continuity of local flux interfaces 2 and 3. These three equations constitute a system of equations

$$\mathbf{A}\mathbf{v} = \mathbf{B}\mathbf{u}, \dots \dots \dots \dots \dots \dots \dots \dots (16)$$

where $\mathbf{A}$ is a 3×3 matrix, $\mathbf{B}$ is a 3×4 matrix, $\mathbf{v}$ is a vector of the potential at the interface midpoints, and $\mathbf{u}$ is a vector of node pressures; i.e.,

$$\mathbf{v} = \left[\bar{u}_1, \bar{u}_2, \bar{u}_3\right]^{\mathrm{T}},$$
$$\mathbf{u} = \left[u_1, u_2, u_3, u_4\right]^{\mathrm{T}}. \dots \dots \dots \dots \dots \dots (17)$$

From the local system of flux-continuity equations, we may further express the vector consisting of the fluxes across the three interfaces as

$$\mathbf{f} = \mathbf{C}\mathbf{v} + \mathbf{D}\mathbf{u}, \dots \dots \dots \dots \dots \dots \dots (18)$$

where the 3×3 matrix $\mathbf{C}$ and the 3×4 matrix $\mathbf{D}$ follow in a straightforward manner. Finally, the transmissibility matrix $\mathbf{T}$ is obtained for the L-stencil fluxes through

$$\mathbf{T} = \mathbf{C}\mathbf{A}^{-1}\mathbf{B} + \mathbf{D}, \dots \dots \dots \dots \dots \dots \dots (19)$$

provided that the matrix $\mathbf{A}$ is nonsingular. $\mathbf{T} = \{t_{ij}\}$ is a 3×4 matrix, and each row of it contains the transmissibilities of the corresponding subinterface. We will give analytical expressions for the transmissibilities in the case of uniform parallelepiped grids on homogeneous media.

Noncentered L-Stencils

A noncentered L-stencil for the right subinterface of Fig. 2 is shown in **Fig. 3.** Again, four cells interact, and, although fluxes may be calculated for the three subinterfaces in the L-stencil, we store only the transmissibilities of the central interface, shown as shaded in Fig. 3.

The local system of flux-continuity equations will be similar to the local system obtained for the ordinary configuration and may
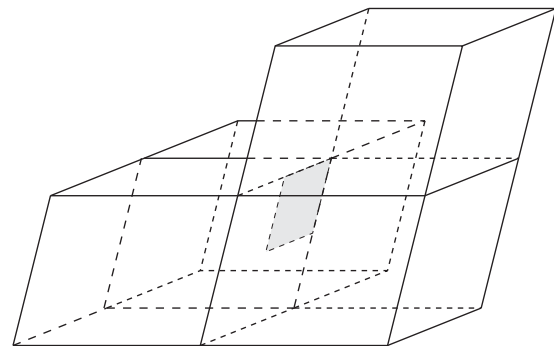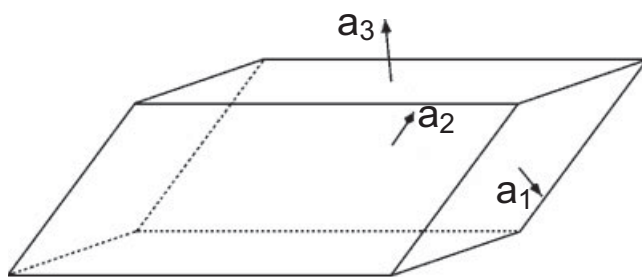

Fig. 3—Noncentered L-stencil.

Fig. 4—The normal vectors a_1, a_2, and a_3.

Fig. 5—Local numbering in the interaction volume.

be expressed in terms of the node pressures and three potentials at the interface midpoints. We omit the details for the derivations of the transmissibility calculations for this case.

Selection Criterion

There are now four different ways of calculating the transmissibilities for each subinterface contained in an interaction region; see Fig. 1. There will be two possible transmissibility sets when centered L-stencils are used and two different transmissibility sets when noncentered L-stencils are used. Similar to the 2D implementation of the L-method in Aavatsmark et al. (2008), we will select one of these four sets for each subinterface on the basis of a property that we believe is important for constructing discrete fluxes with good robustness.

It seems natural that the sign of the transmissibility coefficients associated with the cells on each side of the subinterface should be the same. For homogeneous media and uniform parallelepiped grids for which the deviation from **K**-orthogonality is not too large, this may be accomplished by the following selection criterion. Denote the two central cells that separate the interface for which we compute the flux by 1 and 2. For each L-stencil I, we choose to compute the quantity

$$s_I = |t_1 - t_2|, \dots \dots \dots \dots \dots \dots \dots \dots \dots \dots (20)$$

where t_j is the transmissibility of cell j, $j = 1, 2$. We choose the set of transmissibilities that yields the smallest s_I value.

In the next section, we will show that, for homogeneous media and uniform parallelepiped grids with inequality (Eq. 28) fulfilled, this criterion always yields transmissibilities with the sign property mentioned earlier. However, we will use the selection criterion (Eq. 20) for general grids and media. Obviously, the selection criterion does not guarantee any sign property in the general case, but numerical tests indicate favorable convergence and monotonicity properties also in this case.

The underlying idea of the criterion (Eq. 20) is that the transmissibility coefficients of the two central cells should be as little dominating as possible. However, the reason for choosing this criterion is the observation that it yields the desired sign property of the transmissibility coefficients in the simplest cases. Also, in 2D, this selection criterion yields the largest possible monotonicity region for homogeneous media and uniform parallelogram grids (Aavatsmark et al. 2008).

Uniform Parallelepiped Grid

In this section, we assume a uniform parallelepiped grid on a homogeneous medium. For this case, we can derive analytical expressions for the stencils of the L-method.

To derive these stencils, it is convenient to introduce the quantities a, b, c, d, e, and f, defined by

$$\begin{bmatrix} a & d & e \\ d & b & f \\ e & f & c \end{bmatrix} = \frac{1}{V} [\mathbf{a}_1, \mathbf{a}_2, \mathbf{a}_3]^T \mathbf{K} [\mathbf{a}_1, \mathbf{a}_2, \mathbf{a}_3]. \dots \dots \dots \dots (21)$$
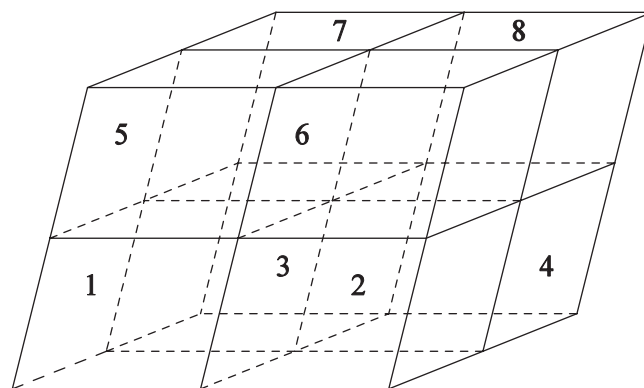
Here, V is the volume of a parallelepiped cell, and $\mathbf{a}_1$, $\mathbf{a}_2$, and $\mathbf{a}_3$ are the cell normals in i, j, and k directions, respectively, the length of each normal being equal to the area of the parallelepiped face to which it is normal. These normal vectors are shown in **Fig. 4.**

Because the right-hand side of Eq. 21 is a congruence transformation, it follows that $a > 0$, $b > 0$, and $c > 0$.

Fig. 5 shows an interaction volume in the grid. The volume contains eight interacting cells. They are numbered locally, as shown in Fig. 5. These eight cells determine the fluxes through the 12 subinterfaces of the interaction volume. For each subinterface, there are four possible L-stencils for computation of the flux through the subinterface. For the lower-back interface of the interaction volume, the four possible L-stencils are shown in Fig. 1. We index the four L-stencils of a subinterface with A, B, C, and D; see Fig. 1. The flux expressions of each of the L-stencils are given by

$$f_A = \frac{1}{4}[du_1 + (a-d+e)u_3 - au_4 - eu_7],$$

$$f_B = \frac{1}{4}[du_2 + au_3 - (a+d-e)u_4 - eu_8],$$

$$f_C = \frac{1}{4}[du_2 + (a+e)u_3 - (a+d)u_4 - eu_7],$$

$$\text{and } f_D = \frac{1}{4}[du_1 + (a-d)u_3 - (a-e)u_4 - eu_8]. \dots \dots \dots (22)$$

Let us compute the indicator $s = |t_3 - t_4|$ (Eq. 20). (Here, we apply the local numbering of the interaction volume, shown in Fig. 5; hence, the central cells of the lower-back subinterface have indices 3 and 4.) For each of the Eq. 22 flux expressions, respectively, the indicator s has the value

$$s_A = \frac{1}{4}(2a - d + e),$$

$$s_B = \frac{1}{4}(2a + d - e),$$

$$s_C = \frac{1}{4}(2a + d + e),$$

$$\text{and } s_D = \frac{1}{4}(2a - d - e). \dots \dots \dots \dots \dots \dots \dots \dots (23)$$

Here, we would like the coefficients of Cells 1 and 7 to be positive and the coefficients of Cells 2 and 8 to be negative. For the 2D L-method, this sign preference guarantees that the monotonicity region of the method becomes as large as possible in the parameter space (Nordbotten et al. 2007; Aavatsmark et al. 2008). Applying the selection criterion (Eq. 20) to the expressions (Eq. 23), the appropriate L-stencil of Fig. 1 is chosen as shown in **Table 1.** The selection depends on the sign of d and e as shown in the table, and inspection of the coefficients in the subinterface flux

TABLE 1—CHOICE OF L-STENCIL OF FIG. 1 BY THE SELECTION CRITERION (Eq. 20) APPLIED TO THE EXPRESSION (Eq. 23)			
$d > 0, e > 0$	$d > 0, e < 0$	$d < 0, e > 0$	$d < 0, e < 0$
D	A	B	C

expressions (Eq. 22) shows that the sign preferences mentioned are preserved.

In the same way, we may compute the flux expressions for the four L-stencils of each subinterface in the interaction volume. Using the selection criterion (Eq. 20), the correct L-stencil is chosen. However, while the selection criterion always yields transmissibility coefficients of the noncentral cells with the desired sign, the transmissibility coefficients of the central cells are not always as desired. Correct sign of these coefficients can be guaranteed only as long as the M-matrix inequalities (Eq. 28) are fulfilled.

Having found the correct L-stencil for each of the 12 subinterfaces, we may compute the flux expressions of the entire interfaces. Let f_1, f_2, and f_3 be the flux of an entire interface in the i, j, and k direction, respectively. The derivation gives, for the flux in the i direction,

$$f_1 = \left(a - \frac{|d|+|e|}{2}\right)\left(u_{i,j,k} - u_{i+1,j,k}\right) + \frac{|d|+d}{4}\left(u_{i,j-1,k} - u_{i+1,j+1,k}\right)$$
$$+ \frac{|d|-d}{4}\left(u_{i,j+1,k} - u_{i+1,j-1,k}\right) + \frac{|e|+e}{4}\left(u_{i,j,k-1} - u_{i+1,j,k+1}\right)$$
$$+ \frac{|e|-e}{4}\left(u_{i,j,k+1} - u_{i+1,j,k-1}\right);$$

$$\dots \dots \dots \dots \dots \dots \dots \dots (24)$$

for the flux in the j direction,

$$f_2 = \left(b - \frac{|d|+|f|}{2}\right)\left(u_{i,j,k} - u_{i,j+1,k}\right) + \frac{|d|+d}{4}\left(u_{i-1,j,k} - u_{i+1,j+1,k}\right)$$
$$+ \frac{|d|-d}{4}\left(u_{i+1,j,k} - u_{i-1,j+1,k}\right) + \frac{|f|+f}{4}\left(u_{i,j,k-1} - u_{i,j+1,k+1}\right)$$
$$+ \frac{|f|-f}{4}\left(u_{i,j,k+1} - u_{i,j+1,k-1}\right);$$

$$\dots \dots \dots \dots \dots \dots \dots \dots (25)$$

and, for the flux in the k direction,

$$f_3 = \left(c - \frac{|e|+|f|}{2}\right)\left(u_{i,j,k} - u_{i,j,k+1}\right) + \frac{|e|+e}{4}\left(u_{i-1,j,k} - u_{i+1,j,k+1}\right)$$
$$+ \frac{|e|-e}{4}\left(u_{i+1,j,k} - u_{i-1,,k+1}\right) + \frac{|f|+f}{4}\left(u_{i,j-1,k} - u_{i,j+1,k+1}\right)$$
$$+ \frac{|f|-f}{4}\left(u_{i,j+1,k} - u_{i,j-1,k+1}\right).$$

$$\dots \dots \dots \dots \dots \dots \dots \dots (26)$$

Each of the flux stencils is a 10-point stencil. However, because one of the expressions $|d|+d$ or $|d|-d$ vanishes and similarly with the expressions for e and f, each of the flux stencils reduces to a six-point stencil. The cells of the flux stencils for the case $d < 0$, $e < 0$, and $f < 0$ are shown in **Fig. 6.**
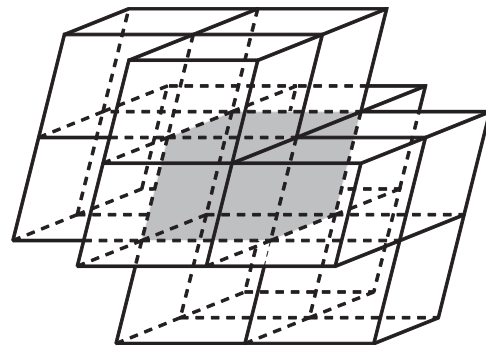
The flux stencils determine the cell stencil. It reads

$$- \int_{\Omega_{i,j,k}} \text{div}\left(\mathbf{K} \text{ grad } u\right)d\tau \approx$$

$$2\left(a+b+c-|d|-|e|-|f|\right)u_{i,j,k} - \left(a-|d|-|e|\right)\left(u_{i-1,j,k} + u_{i+1,j,k}\right)$$
$$- \left(b-|d|-|f|\right)\left(u_{i,j-1,k} + u_{i,j+1,k}\right) - \left(c-|e|-|f|\right)\left(u_{i,j,k-1} + u_{i,j,k+1}\right)$$
$$- \frac{|d|+d}{2}\left(u_{i-1,j-1,k} + u_{i+1,j+1,k}\right) - \frac{|d|-d}{2}\left(u_{i-1,j+1,k} + u_{i+1,j-1,k}\right)$$
$$- \frac{|e|+e}{2}\left(u_{i-1,j,k-1} + u_{i+1,j,k+1}\right) - \frac{|e|-e}{2}\left(u_{i+1,j,k-1} + u_{i-1,j,k+1}\right)$$
$$- \frac{|f|+f}{2}\left(u_{i,j-1,k-1} + u_{i,j+1,k+1}\right) - \frac{|f|-f}{2}\left(u_{i,j-1,k+1} + u_{i,j+1,k-1}\right).$$

$$\dots \dots \dots \dots \dots \dots \dots \dots (27)$$

As Eq. 27 shows, the cell stencil is a 19-point stencil. As for the flux stencils, however, because of vanishing coefficients, it reduces to a 13-point stencil. The cells of the cell stencil for the case $d < 0$, $e < 0$, and $f < 0$ are shown in **Fig. 7.**

Eq. 27 shows that the matrix of coefficients is an M-matrix if

$$|d|+|e| \le a,$$
$$|d|+|f| \le b,$$
$$\text{and } |e|+|f| \le c. \quad \dots \dots \dots \dots \dots \dots \dots \dots (28)$$

These inequalities are not only sufficient but are also necessary for monotonicity. This is easily seen by applying the method to a 1D strip of cells, using homogeneous Dirichlet boundary conditions. From Eq. 21, it follows that $d = e = f = 0$ for **K**-orthogonal grids. Hence, the inequalities (Eq. 28) will be satisfied for grids

Fig. 7—Cells of the cell stencil for the case $d < 0$, $e < 0$, $f < 0$.

Fig. 6—Cells of the flux stencils for the case $d < 0$, $e < 0$, and $f < 0$; (a) f_1, (b) f_2, (c) f_3. Each of the stencils contains six cells.

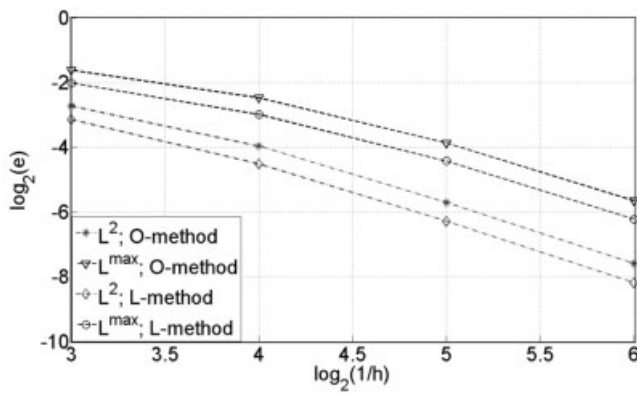Fig. 8—Pressure convergence for parallelepiped grids; both L^2 and L^{max} rates approaching second order.
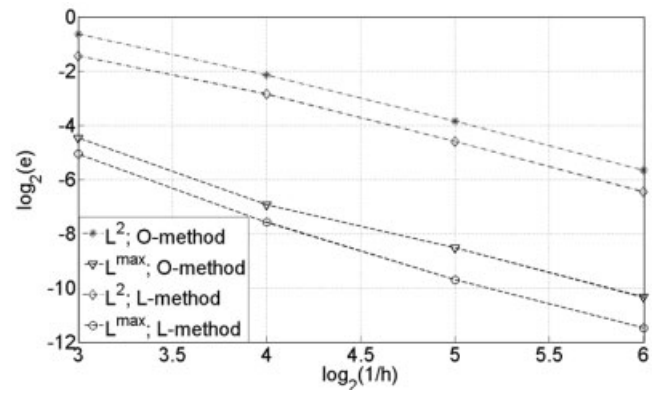

Fig. 9—Normal velocity convergence for parallelepiped grids. Second-order convergence for both methods and both norms used. Max/norm results for normal velocities are scaled.

that are close to **K**-orthogonal. Monotonicity of MPFA methods in 3D is a topic of ongoing research. The associated 2D method derived in Nordbotten et al. (2007) is optimal in the sense that no other control-volume method using only the neighboring cells in the stencil has a larger monotonicity region. However, in 3D no such results exist.

Numerical Results

Here, we test our L-method implementation on various grids and media that represent challenges in reservoir simulation. We solve the model equation

$$Lu = Q, \dots \dots \dots \dots \dots \dots \dots (29)$$

where the operator L is given by Eq. 1. We apply either an isotropic medium or a medium with a permeability tensor possessing two equal eigenvalues and one that is different. A general form of the permeability tensor in the last case is given by

$$\mathbf{K} = \mathbf{R}^T \mathbf{\Lambda} \mathbf{R}, \dots \dots \dots \dots \dots \dots \dots (30)$$

where $\mathbf{\Lambda} = \mathrm{diag}(\lambda, \lambda, \lambda_3)$, and

$$\mathbf{R} = \begin{bmatrix} \cos\psi & \sin\psi & 0 \\ -\cos\theta\sin\psi & \cos\theta\cos\psi & \sin\theta \\ \sin\theta\sin\psi & -\sin\theta\cos\psi & \cos\theta \end{bmatrix}. \dots \dots \dots \dots (31)$$

Here, ψ is the azimuth of the strike direction of the isotropic plane measured from the x axis, and θ is the dip angle of the isotropic plane.

With the parameters $\psi = 135°$, $\theta = \arctan(\sqrt{2}) \approx 54.7°$, $\lambda = 1$, and $\lambda_3 = 3s+1$, a permeability matrix on a simple form appears:

$$\mathbf{K} = \begin{bmatrix} s+1 & s & s \\ s & s+1 & s \\ s & s & s+1 \end{bmatrix}. \dots \dots \dots \dots \dots \dots (32)$$

This permeability tensor yields an anisotropy ratio $\kappa = 3s+1$. The eigenvector associated with the eigenvalue $3s+1$ is $[1, 1, 1]^T$. The two eigenvectors associated with the eigenvalue 1 span a plane that stands orthogonal to this vector.

If, instead, $\psi = 45°$ and the parameters θ, λ, and λ_3 are as defined previously, the permeability matrix

$$\mathbf{K} = \begin{bmatrix} s+1 & -s & s \\ -s & s+1 & -s \\ s & -s & s+1 \end{bmatrix}. \dots \dots \dots \dots (33)$$

appears. The anisotropy ratio κ is the same as it was previously. Here, however, the eigenvector associated with the eigenvalue $3s+1$ is $[1, -1, 1]^T$.

The test cases described in the next sections will make use of the permeability tensors (Eqs. 30 through 33).

Convergence

We test the convergence of the L-method by comparing the errors with the O-method (Aavatsmark et al. 1998). The tests are performed for both homogeneous and heterogeneous media. Some challenging cases are especially investigated.

Homogeneous Case. In our first test cases, the medium is homogeneous and isotropic, and we apply the analytical solution

$$u(x,y,z) = \sin\left(\sqrt{2}\pi x\right)\sinh\left(\pi y\right)\sinh\left(\pi z\right). \dots \dots \dots (34)$$

This solution is applied for the convergence tests shown in **Figs. 8 through 13.** The implementation makes use of the selection criterion (Eq. 20) for L-stencils discussed previously. For all convergence examples presented here, Dirichlet boundary conditions are used.

We first present the numerical results for uniform parallelepipeds (in 3D). In Figs. 8 and 9, we have plotted the L^2 errors and L^{max} errors for the pressure and normal velocity for both the O-method and the L-method. The parallelepiped domain used here is described by the parameters in Eq. 21 whose values are $a = 1.5$, $b = c = 1$, $d = e = -0.5$, and $f = 0$.

As seen from the plots, the convergence rates are approaching second order for both pressure and normal velocity for both methods in both L^2 norm and L^{max} norm. Note that the error constant is significantly smaller for the L-method here.

Figs. 10 and 11 show convergence results for the O-method and L-method on sequences of grid refinements of **K**-orthogonal, unit-aspect-ratio grids, where random perturbations are introduced of the same order as the grid cell size on all refinement levels. Such grids are referred to as "rough" grids in the literature; see Klausen and Winther (2006b).

The convergence order is maintained (at second order) for the pressure, whereas the rate for the normal velocities drops to first order. As seen from the plot, the pressure is almost identical for the L-method and the O-method, whereas normal velocities are marginally better for the O-method.

As for the 2D cases (Aavatsmark et al. 2008), we next study the effect of grid aspect ratios far away from unity. We have performed convergence tests for the preceding analytical solution where the refinements still contain random perturbations of the same order as the cell size. The grids are rough perturbations of **K**-orthogonal grids where the grid has been compressed by a factor 1/100 in the z direction. The convergence behavior is depicted in Figs. 12 and 13.
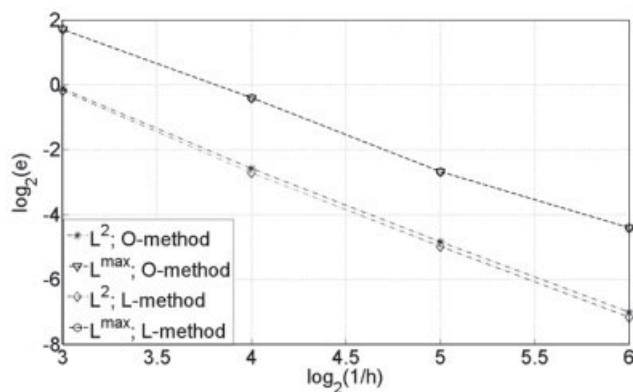
Fig. 10—Pressure convergence for L-method and O-method for rough-grid refinements and grid aspect ratio of approximately unity. Roughly second-order convergence is observed for both methods and both norms. The max/norm curves are overlapping.

Fig. 11—Normal velocity convergence for L-method and O-method for rough grid and grid aspect ratio of approximately unity. First-order convergence is observed for both methods and both norms. Normal velocities are scaled for max/norm calculations.

The convergence rates for the L-method are reduced compared to the random refinements of grids with aspect ratios close to unity. In particular, the observed rate for the last refinement is $h^{1.1}$ for the pressure and $h^{0.8}$ for the normal velocities for the L-method. The O-method does not converge for this case. These results are in agreement with the 2D results in Aavatsmark et al. (2008). Note that the refinement levels presented here are coarser than those for the 2D examples in Aavatsmark et al. (2008) because of the increased computational efforts needed for 3D simulation. Also note that, because the extension in the z direction is only one-hundredth of the extension in the previous example (with unit aspect ratio), the solution is much smaller. This explains why the L-method curves in Fig. 12 end at a much smaller value than do the L-method curves of Fig. 10.

Another interesting feature of the rough simulation grids with grid aspect ratios far away from unity is that the condition number of the resulting coefficient matrix for the discretization behaves differently for the L-method and the O-method. In **Fig. 14,** we have plotted the behavior of the coefficient matrix for the various refinement levels used in the convergence tests. Whereas the condition number for the L-method discretization stays reasonably small and does not increase unexpectedly, the O-method discretization feels a strong effect of the large grid aspect ratio.

It should be noted that, because of the large condition numbers seen for the O-method, the numerical results may be affected to some degree by the linear solver used for the discrete problem. This could possibly explain the rapid divergence seen for the O-method for the last refinement levels. From a practical perspective, the relatively small condition numbers for the L-method is a beneficiary feature.

The condition number of the matrix of coefficients appears to be sensitive to the permeability tensor. We have tested the 2-norm condition number of the matrix of coefficients for L-method discretization of Eq. 29 with homogeneous Dirichlet boundary conditions. The permeability matrix is given by Eq. 30, with anisotropy ratio $\kappa = 10$. We have tested cases with azimuth $\psi \in [0°, 45°]$ for the dip angles $\theta = 81°$ and $\theta = 72°$. For all test cases, we have applied a uniform $17 \times 17 \times 17$ grid with cubic grid cells. The results are shown in **Fig. 15.**

Fig. 13—Normal velocity convergence for L-method and O-method for an aspect ratio of 1/100. Reduced convergence rates observed in initial refinements for the L-method. Normal velocities for the O-method seem to diverge.
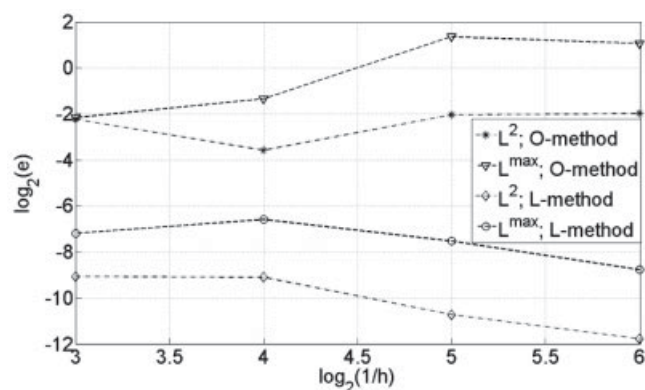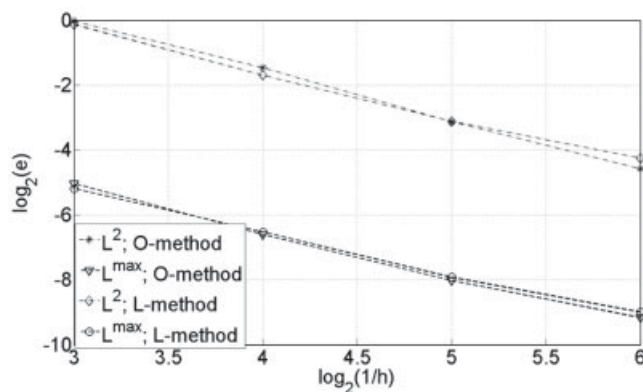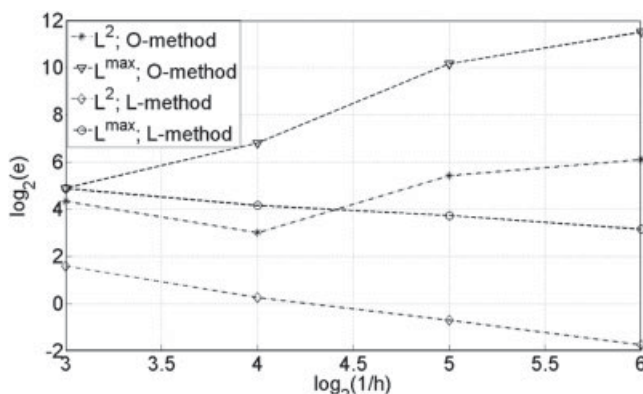

Fig. 12—Pressure convergence for L-method and O-method for an aspect ratio of 1/100. Reduced convergence rates are observed in initial refinements for the L-method, whereas convergence cannot be established for the O-method.
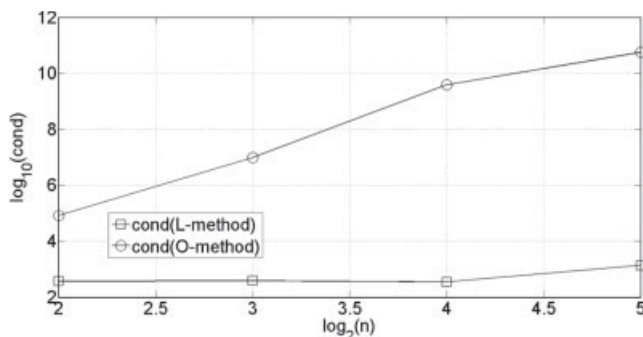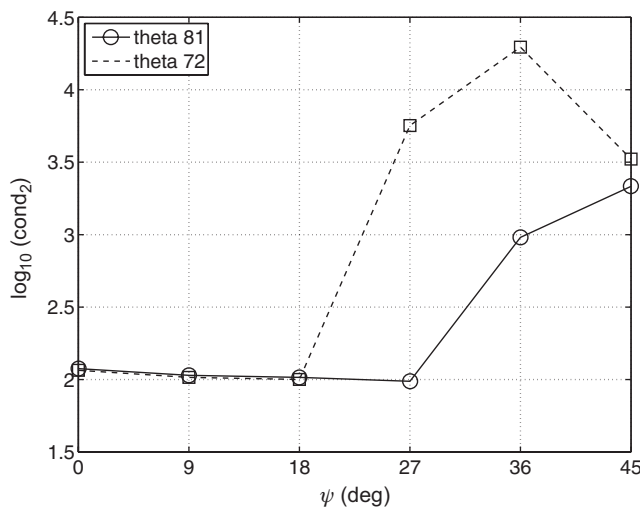

Fig. 14—Condition number of coefficient matrix vs. grid refinement for the L-method and O-method discretizations. Aspect ratio is 1/100. Condition number and increase vs. refinement is much smaller for L-method than for O-method.

Fig. 15—Condition number of matrix of coefficients as function of azimuth ψ and dip angle θ of isotropic plane, L-method. Homogeneous Dirichlet boundary conditions. Permeability tensor given by Eq. 30. Anisotropy ratio $\kappa = 10$. Solid curve $\theta = 81°$. Dashed curve $\theta = 72°$.

Fig. 15 shows that the condition number stays low as long as the eigenvector of the eigenvalue different from the other two is close to one of the grid directions. For dip angle $\theta = 81°$, this eigenvector is 9° over the x–y plane. In this case, for rotations in the x–y plane up to $\psi = 27°$, the condition number remains low. For dip angle $\theta = 72°$, the eigenvector is 18° over the x–y plane. In this case, the condition number remains low for rotations up to only $\psi = 18°$. The related monotonicity issues will be discussed in a later section.

Heterogeneous Cases. The convergence of the pressure and normal velocities is now studied for the O-method and the L-method for specific examples on heterogeneous media.

Both the L-method and the O-method have the property that they will reproduce piecewise uniform flow exactly. The implementations of both methods are validated by verifying that they reproduce exact pressures and normal velocities on randomly perturbed grids for such cases. For all the grid types employed for the numerical examples, this underlying test is implemented.

An example of piecewise uniform flow is given by the following. Consider the domain $\Omega_1 \cup \Omega_2$ given by the subdomains

$$\Omega_1 = [0,1] \times [0,\tfrac{1}{2}] \times [0,1],$$
$$\text{and } \Omega_2 = [0,1] \times [\tfrac{1}{2},1] \times [0,1]. \quad \ldots \ldots \ldots \ldots \ldots \ldots (35)$$

Assign permeabilities $\mathbf{K}_1$ and $\mathbf{K}_2$ to these subdomains, respectively, where $\mathbf{K}_1 = \mathbf{I} = \text{diag}(1, 1, 1)$ and $\mathbf{K}_2$ is given by Eq. 32 with $s = 1$. It is now readily verified that the piecewise linear (and continuous) potential given by

$$u(x,y,z) = x + y + z, \quad (x,y,z) \in \Omega_1$$
$$\text{and } u(x,y,z) = x - \frac{y}{2} + z + \frac{3}{4}, \quad (x,y,z) \in \Omega_2 \quad \ldots \ldots \ldots \ldots (36)$$

is a solution of Eq. 29 with $Q = 0$ for corresponding boundary conditions. Our implementations of both the O-method and L-method reproduce this solution on randomly perturbed grids.

In the next test case, we again subdivide the domain in the subdomains (Eq. 35) and assign the permeabilities (Eqs. 32 and 33, respectively) to the subdomains Ω_1 and Ω_2. An analytical solution to Eq. 29 with $Q = 0$ is given by

$$u(x,y,z) = y\left[2y^2 - 3(s+1)(x-z)^2\right]. \quad \ldots \ldots \ldots \ldots \ldots (37)$$
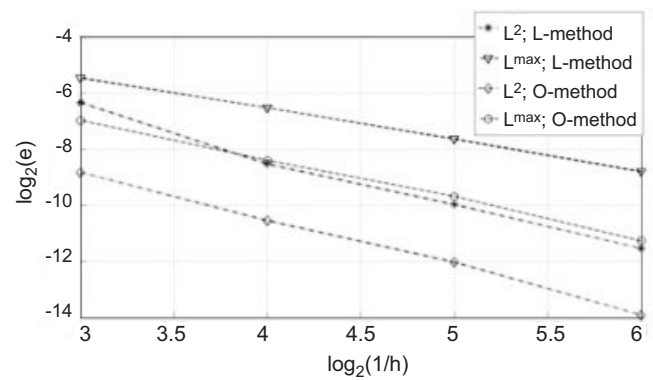
Fig. 16—Pressure convergence for L-method and O-method for rough grid refinements and grid aspect ratio of approximately unity. Heterogeneous medium.

We have tested this solution with $s = 1$. On uniform Cartesian grids (aligning with the inner medium discontinuity at $y = \tfrac{1}{2}$), the O-method is found to have the remarkable property that the solution of the corresponding discrete pressure equation is exact. This is also the case for several other cubic solutions of problems with constant permeability in each of the subdomains Ω_1 and Ω_2. The L-method does not reproduce the solution exactly but does so for solutions of the same form on homogeneous media. At the time of writing, these favorable O-method properties are not fully understood.

Consider now general skewed simulation grids applied to the entire simulation domain. In the convergence tests, the grids are refined randomly and grid perturbations (normal distribution for random function) are introduced on all levels. The plots of **Figs. 16 and 17** show the convergence behavior as the grids are refined for pressures and normal velocities, respectively, for both the O-method and the L-method. Note that the quantity h referred to in the plots is the cell size for the unperturbed grids such that the average cell size for the perturbed grids will deviate a bit from this.

It should be noted that the errors are larger for the L-method for both pressures and fluxes. This is explained by the fact that the O-method reproduces the analytical solution exactly for unperturbed Cartesian grids, whereas the L-method does not do this. When the grids are perturbed, the O-method experiences a gradual increase of errors (increasing with deviation from unperturbed grids), starting from 0, whereas the L-method errors are not 0 in the limit when the grids are unperturbed.

The convergence rates seem to be the same asymptotically for the O-method and the L-method. The observed rates are approximately $h^{1.8}$ for the pressures in the L^2 norm and $h^{1.4}$ for the pressures in the L^∞ norm. This suggests that the asymptotical convergence has not been reached by the refinements employed here.
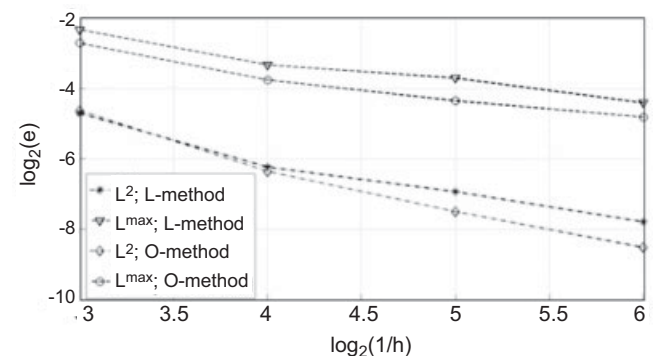
Fig. 17—Normal-velocity convergence for L-method and O-method for rough grid and grid aspect ratio of approximately unity. Heterogeneous medium.
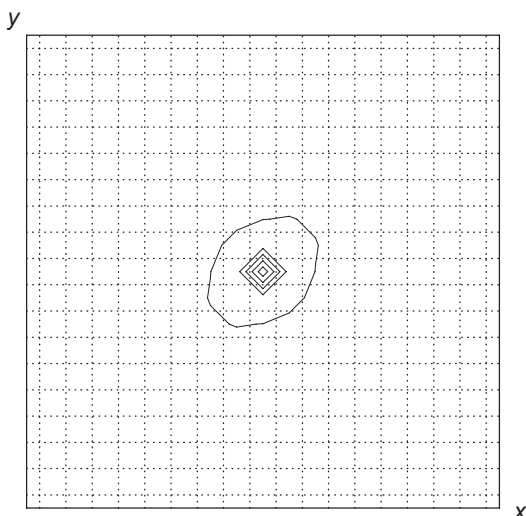
Fig. 18—Potential lines at $u = 4(n–½)$, $n = 1, …, 5$, in a slice at $k = 9$ (midpoint in z direction). Grid lines dotted. Point source. $\kappa = 3$.

Fig. 19—Potential lines at $u = 4(n–½)$, $n = 1, …, 6$, in a slice at $k = 9$ (midpoint in z direction). Grid lines dotted. Point source. $\kappa = 4$.

For the normal velocities in L^2 norm, both the L-method and the O-method seem to achieve asymptotically a convergence order of h^1.

The L^∞ rates of the normal velocities seem to be almost h^1 for both methods, although the observed rates are somewhat lower. This is explained either by possibly reduced regularity of the solution or by the fact that asymptotical convergence is not reached in the refinements used here.

Monotonicity

In this section, we test monotonicity of the L-method for homogeneous media and uniform Cartesian cubic grids. In all test cases, we apply a 17×17×17 grid with cell width $h = 0.01$. In the first test cases, the permeability is given by Eq. 32. The parameters defined in Eq. 21 are then given by
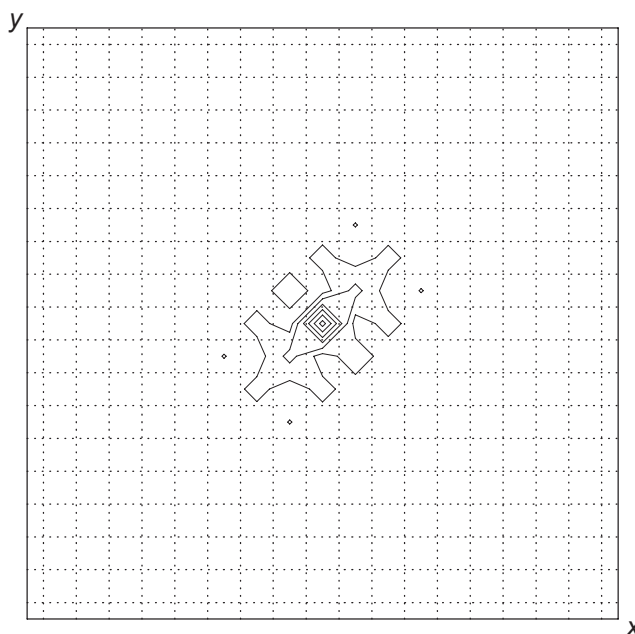
$$a = b = c = h(s+1)$$
$$\text{and } d = e = f = hs . \quad\dots\dots\dots\dots\dots\dots\dots\dots\dots\dots\dots (38)$$

The quantity h is the cell width but may also be seen as a normalization factor of the permeability. From Eq. 28, it follows that the L-method is monotone if and only if $s \leq 1$ (i.e., if and only if the anisotropy ratio $\kappa = 3s+1$ is bounded by $\kappa \leq 4$).

To illustrate the behavior of the L-method, we solve Eq. 29 with the permeability (Eq. 32), using homogeneous Dirichlet boundary conditions (implemented in ghost cells). The source density Q vanishes everywhere except in Cell (9, 9, 9), where the source strength is $Qh^3 = 1$. **Figs. 18 and 19** show the contours of the solution u in a slice at $k = 9$ (midpoint in z direction). In Fig. 18, $\kappa = 3$, while, in Fig. 19, $\kappa = 4$.

The solution for $\kappa = 3$ looks fine, while the solution for $\kappa = 4$ contains valleys running diagonally in the x–y plane. However, the solution is positive for all cells, and there are no local minima. Such valleys start to appear for anisotropy ratios of approximately $\kappa = 3.9$. At $\kappa = 4.1$, the solution contains local minima with negative values. Hence, with point sources, the M-matrix criterion (Eq. 28) gives an almost-sharp bound for the appearance of unacceptable solutions. To be safe, the parameters should stay somewhat below the M-matrix bounds.

A point source in 3D is rather uncommon in reservoir simulation. Therefore, we have tested the behavior of the L-method in case of a line source. The grid, the medium, and the boundary conditions are the same as previously, but now the source density vanishes in all cells except the cells (9, 9, k), $k = 1, …, 17$, where the source strength is $Qh^3 = 1/17$. **Figs. 20 and 21** show the con-

tours of the solution u in a slice at $k = 9$. In Fig. 20, $\kappa = 4$, while, in Fig. 21, $\kappa = 6$. The solution for $\kappa = 4$ looks fine, whereas the solution for $\kappa = 6$ contains oscillations with several local negative minima, the strongest lying on the diagonal $x = y$. This behavior is as expected because the M-matrix conditions are broken. However, a comparison of Figs. 19 and 20 clearly shows that line sources are less challenging with respect to monotonicity than point sources.

The eigenvector $[1, 1, 1]^T$ of the permeability matrix (Eq. 32) points diagonally in the grid, and this is a particularly difficult situation for MPFA methods. More commonly, the principal directions of the permeability tensor are close to the directions of the grid. In the next case, therefore, we make use of the permeability matrix (Eq. 30) with $\psi = \theta = 72°$. For these angles, monotonicity
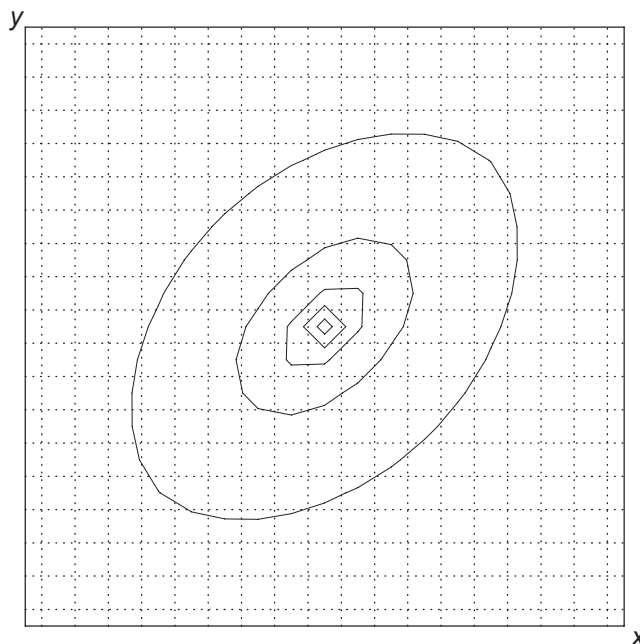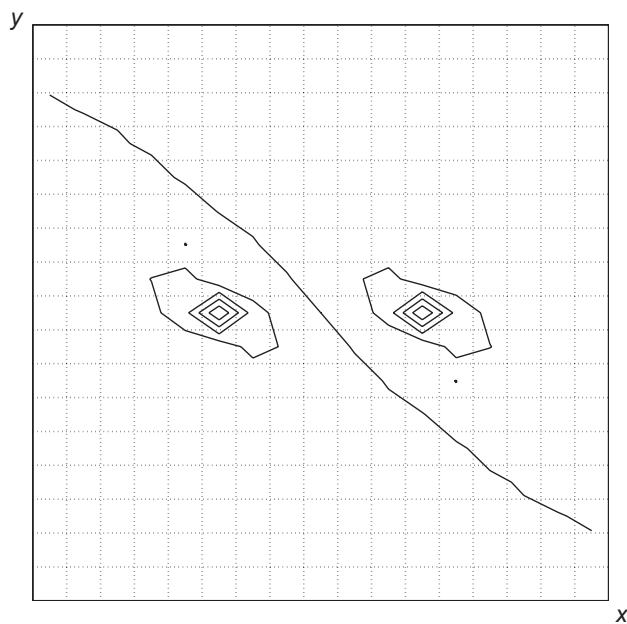

Fig. 20—Potential lines at $u = 0.4(n–½)$, $n = 1, …, 5$, in a slice at $k = 9$ (midpoint in z direction). Grid lines dotted. Line source. $\kappa = 4$.
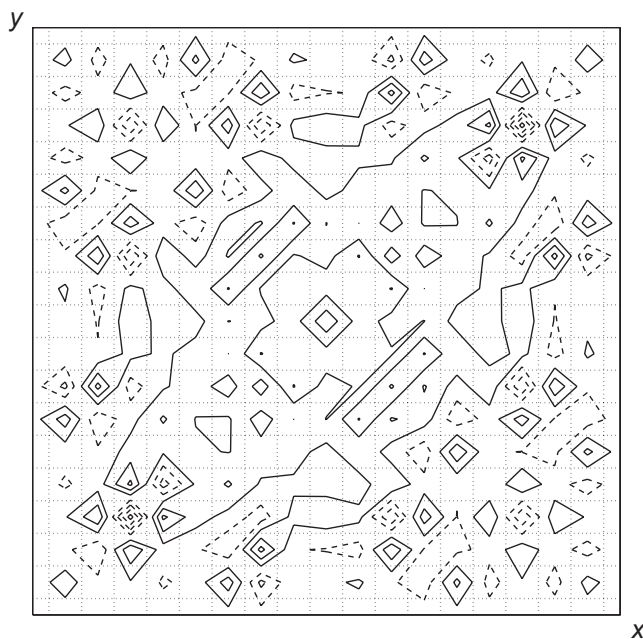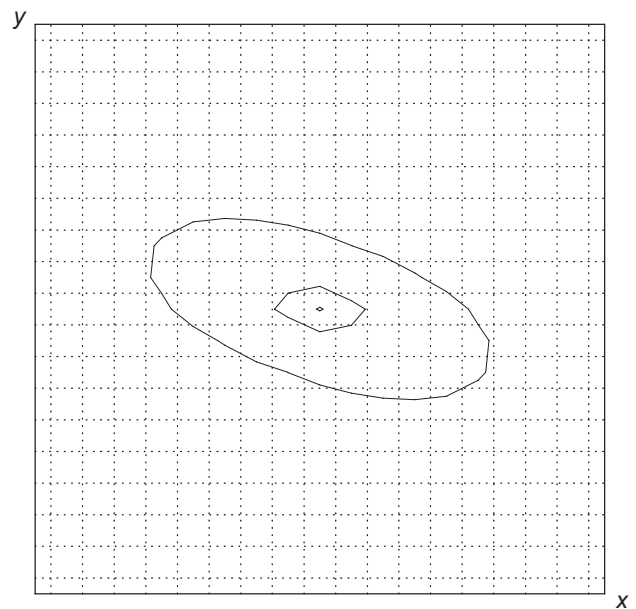
Fig. 21—Potential lines at $u = 0.4(n–½)$, $n = –3, …, 4$, in a slice at $k = 9$ (midpoint in z direction). Solid lines, u positive. Dashed lines, u negative. Grid lines dotted. Line source. $\kappa = 6$. The discrete solution is symmetric, but, because of the plotting routine, the potential lines show a slight asymmetry.

Fig. 22—Potential lines at $u = 0.4(n–½)$, $n = 1, …, 3$, in a slice at $k = 9$ (midpoint in z direction). Grid lines dotted. Line source. K given by Eq. 30 with $\psi = \theta = 72°$. $\kappa = 10$.

(i.e., the M-matrix property) is lost for anisotropy ratios higher than $\kappa = 4.63$. However, for these angles, the solution shows no negative minima, even for $\kappa = 10$. **Fig. 22** shows the contours of the solution u in a slice at $k = 9$ in the case of the same line source as mentioned previously.

We have also tested for the occurrence of extrema on no-flow boundaries. For this purpose, we have solved Eq. 29 with vanishing source density Q and no-flow external boundaries. As we did previously, we use a 17×17×17 grid with cubic cells. The potential is fixed in two internal cells: $u = 0$ in cell (6, 9, 9) and $u = 1$ in cell (12, 9, 9). The solution of this problem must satisfy $u \in [0,1]$. Obviously, the solution is independent of the cell width h.

Using the permeability tensor (Eq. 30) with $\psi = \theta = 72°$, extrema outside the interval [0, 1] appear on the no-flow boundary for high anisotropy ratios κ. However, large internal oscillations may occur for smaller anisotropy ratios. Therefore, it seems that internal oscillations are the dominating problem compared to extrema on no-flow boundaries. This situation is different from the situation in 2D where extrema on no-flow boundaries may occur for nonoscillating solutions (Aavatsmark et al. 2008).

Fig. 23 shows contour lines of the solution u for the no-flow boundary test case described previously with anisotropy ratio $\kappa = 10$. The solution at the boundary lies in the interval [0.44, 0.56].

Nonmatching Grids and LGRs

We will now test the L-method using grids that contain LGRs and nonmatching cells. The first test uses the grid shown in **Fig. 24** with heterogeneous permeability. The gray cells in the figure are assigned $\mathbf{K}_{low} = 10^{-3}\,\mathbf{I}$, and the other cells are assigned $\mathbf{K}_{high} = \mathbf{I}$. For this test, the potential is fixed at unity on the left-forward boundary and at zero on the right-back boundary. No-flow conditions are used for the other boundaries. We will compare the total flux across the domain for this 360-cell grid with results computed using a coarse uniform 8×8×24 = 1,536-cell grid that matches the resolution of the finest LGR level. The reference solution is computed on a fine uniform 64×64×192 = 786,432-cell grid. TPFAs are used for both uniform grids. Relative to the fine grid, the error in the total flux for the LGR grid is 14.3%. The error for the uniform coarse grid is 12.3%. We find the additional 2% error to be acceptable, considering the cell count reduction obtained using LGR.

Fig. 23—Potential lines at $u = 0.1n$, $n = 1, …, 9$, in a slice at $k = 9$ (midpoint in z direction). Grid lines dotted. Line source. No-flow boundaries. K given by Eq. 30 with $\psi = \theta = 72°$. $\kappa = 10$.

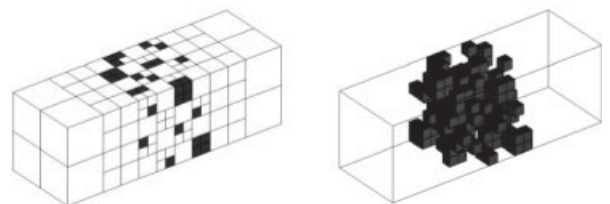Fig. 24—Grid with LGRs used in the heterogeneous test case. The exterior shell of the grid is shown on the left, and the locations of the low-permeability cells are shown on the right. The total number of cells in the grid is 360, and the finest level corresponds to an 8×8×24 = 1,536-cell grid.

Fig. 25—Nonmatching grid.

Fig. 26—Convergence behavior of pressure on nonmatching grid. n is the cube root of the number of degrees of freedom.
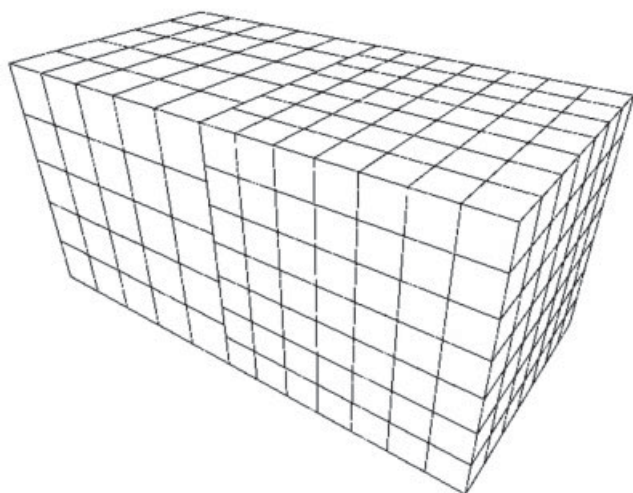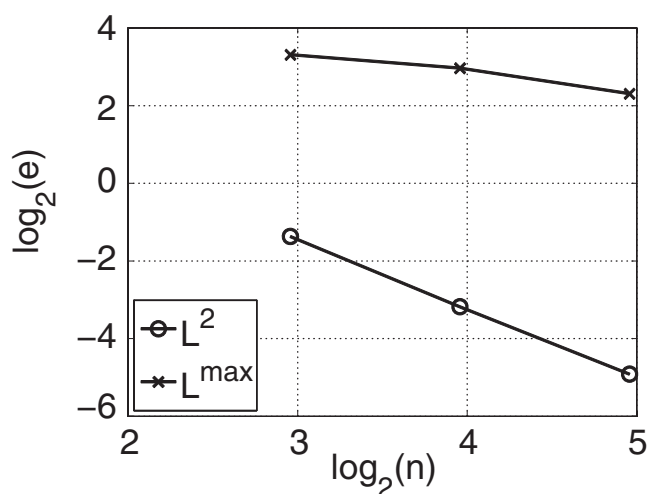

Fig. 27—Convergence behavior of normal velocity on nonmatching grid. n is cube root of the number of degrees of freedom.

Fig. 28—Two-phase flow with LGR. Saturation contours. Horizontal cross section. No gravity.

Next, we apply the centered L-stencil to the simple nonmatching grid shown in **Fig. 25;** see Lipnikov et al. (2006). We test the convergence for the solution (Eq. 34) in an isotropic and a homogeneous medium. Starting from a mesh size of $h_1 = 5$ and $h_2 = 7$, where h_1 is the mesh size for the left LGR and h_2 for the right, a sequence of refined meshes is constructed by doubling the mesh size in each coordinate direction. Convergence is plotted against the cube root n of the total number of grid cells. Pressure is given in **Fig. 26** and normal velocity in **Fig. 27.** The L^2 convergence order of both pressure and normal velocity is 1.7 at the last refinement level. However, the curves in Fig. 26 indicate a higher asymptotic order for the pressure.

Finally, we test two-phase flow over a series of 3D LGRs shown in **Fig. 28.** Water is injected from the center of the leftmost LGR, and a producer is located at the center of the rightmost LGR. While the LGRs are uniform 3D, the plot shows just a 2D intersection along the x and y axis because gravity is not included. Saturation contours are given, and they exhibit no significant orthogonality errors.

Summary and Conclusions

This paper has discussed the development and extension of the MPFA L-method to 3D. A derivation of the method is given together with a possible algorithm for choosing the best L-stencils for subinterfaces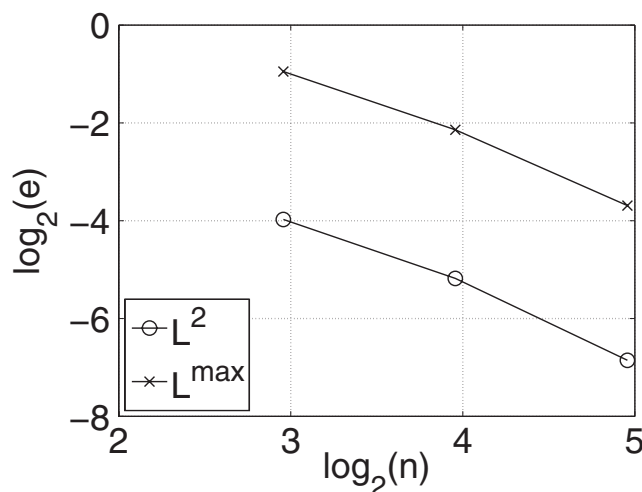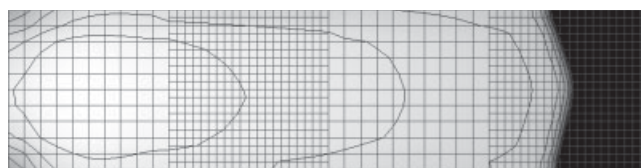 of grid cells. The discretization ideas are discussed for simulation grids with matching grid cells and grids that contain faults or LGRs. Analytical transmissibilities are supplied for uniform parallelepipeds on homogeneous media. It is shown how the resulting cell stencil for the L-method will always be a 13-point stencil (with possible reductions) for these grids. Numerical results are supplied that show excellent convergence properties of the method on challenging grids when Dirichlet conditions are used. Analogously to the 2D implementation of the method, the method is robust for rough grids where the grid aspect ratios are far away from unity. Convergence is established for the L-method for cases where the O-method fails to converge. The L-method, like all other MPFA methods, is conditionally monotone. Test runs with parameters outside the monotonicity region indicate that, for strongly nonlinear solutions, the method should not be used outside its monotonicity region. Further, we have provided convergence results for nonmatching grids and have demonstrated excellent behavior for LGRs.

Nomenclature

f = flux
$\mathbf{K}$ = permeability tensor
t = transmissibility
u = pressure
θ = dip angle of isotropic plane
κ = anisotropy ratio
ψ = azimuth of strike direction of isotropic plane

References

Aavatsmark, I. 2002. An Introduction to Multipoint Flux Approximations for Quadrilateral Grids. *Computational Geosciences* **6** (3–4): 405–432. doi: 10.1023/A:1021291114475.

Aavatsmark, I. 2007. Interpretation of a two-point flux stencil for skew parallelogram grids. *Computational Geosciences* **11** (3): 199–206. doi: 10.1007/s10596-007-9042-1.

Aavatsmark, I. and Eigestad, G.T. 2006. Numerical convergence of the MPFA O-method and U-method for general quadrilateral grids. *Int. J. Numer. Methods Fluids* **51** (9–10): 939–961. doi: 10.1002/fld.1096.

Aavatsmark, I., Barkve, T., and Mannseth, T. 1998. Control-Volume Discretization Methods for 3D Quadrilateral Grids in Inhomogeneous, Anisotropic Reservoirs. *SPE J.* **3** (2): 146–154. SPE-38000-PA. doi: 10.2118/38000-PA.

Aavatsmark, I., Barkve, T., Bøe, Ø., and Mannseth, T. 1996. Discretization on non-orthogonal, quadrilateral grids for inhomogeneous, anisotropic media. *J. Comput. Phys.* **127** (1): 2–14. doi: 10.1006/jcph.1996.0154.

Aavatsmark, I., Eigestad, G.T., and Klausen, R.A. 2006a. Numerical convergence of the MPFA O-method for general quadrilateral grids in two and three dimensions. In *Compatible Spatial Discretizations*, ed. D.N. Arnold, P.B. Bochev, R.B. Lehoucq, R.A. Nicolaides, and M. Shashkov, Vol. 142, 1–21. New York: The IMA Volumes in Mathematics and its Applications, Springer.

Aavatsmark, I., Eigestad, G.T., Klausen, R.A., Wheeler, M.F., and Yotov, I. 2007. Convergence of a symmetric MPFA method on quadrilateral grids. *Computational Geosciences* **11** (4): 333–345. doi: 10.1007/s10596-007-9056-8.

Aavatsmark, I., Eigestad, G.T., Mallison, B.T., and Nordbotten, J.M. 2008. A compact multipoint flux approximation method with improved robustness. *Numer. Methods Partial Diff. Eqns.* **27** (5): 1329–1360. doi: 10.1002/num.20320.

Aavatsmark, I., Eigestad, G.T., Nordbotten, J.M. 2006b. A Compact MPFA Method with Improved Robustness. Paper B019 presented at the 10th European Conference on the Mathematics of Oil Recovery (ECMOR X), Amsterdam, 4–7 September.

Aavatsmark, I., Reiso, E., and Teigland, R. 2001a. Control Volume Discretization Method for Quadrilateral Grids with Faults and Local Refinements. *Computational Geosciences* **5** (1): 1–23. doi: 10.1023/A:1011601700328.

Aavatsmark, I., Reiso, E., Reme, H., and Teigland, R. 2001b. MPFA for Faults and Local Refinements in 3D Quadrilateral Grids With Application to Field Simulations. Paper SPE 66356 presented at the SPE Reservoir Simulation Symposium, Houston, 11–14 February. doi: 10.2118/66356-MS.

Chen, Q.-Y., Wan, J., Yang, Y., and Mifflin, R.T. 2008. Enriched multipoint flux approximation for general grids. *J. Comput. Phys.* **227** (3): 1701–1721. doi: 10.1016/j.jcp.2007.09.021.

Edwards, M.G. 2002. Unstructured, Control-Volume Distributed, Full-Tensor Finite Volume Schemes with Flow Based Grids. *Computational Geosciences* **6** (3–4): 433–452. doi: 10.1023/A:1021243231313.

Edwards, M.G. and Rogers, C.F. 1998. Finite volume discretization with imposed flux continuity for the general tensor pressure equation. *Computational Geosciences* **2** (4): 259–290. doi: 10.1023/A:1011510505406.

Edwards, M.G. and Zheng, H. 2008. A quasi-positive family of continuous Darcy-flux finite-volume schemes with full pressure support. *J. Comput. Phys.* **227** (22): 9333–9364. doi: 10.1016/j.jcp.2008.05.028.

Eigestad, G.T. and Klausen, R.A. 2005. On the convergence of the multipoint flux approximation O-method: Numerical experiments for discontinuous permeability. *Numer. Methods Partial Diff. Eqns.* **21** (6): 1079–1098. doi: 10.1002/num.20079.

Keilegavlen, E., Nordbotten, J.M., and Aavatsmark, I. 2009. Sufficient criteria are necessary for monotone control volume methods. *Appl. Math. Lett.* **22** (8): 1178–1180. doi: 10.1016/j.aml.2009.01.048.

Klausen, R.A. and Winther, R. 2006a. Convergence of multipoint flux approximations on quadrilateral grids. *Numer. Methods Partial Diff. Eqns.* **22** (6): 1438–1454. doi: 10.1002/num.20158.

Klausen, R.A. and Winther, R. 2006b. Robust convergence of multi point flux approximation on rough grids. *Numerische Mathematik* **104** (3): 317–337. doi: 10.1007/s00211-006-0023-4.

Lipnikov, K., Shashkov, M., and Svyatskiy, D. 2006. The mimetic finite difference discretization of diffusion problem on unstructured polyhedral meshes. *J. Comput. Phys.* **211** (2): 473–491. doi: 10.1016/j.jcp.2005.05.028.

Nordbotten, J.M. and Aavatsmark, I. 2005. Monotonicity conditions for control volume methods on uniform parallelogram grids in homogeneous media. *Computational Geosciences* **9** (1): 61–72. doi: 10.1007/s10596-005-5665-2.

Nordbotten, J.M., Aavatsmark, I., and Eigestad, G.T. 2007. Monotonicity of control volume methods. *Numerische Mathematik* **106** (2): 255–288. doi: 10.1007/s00211-006-0060-z.

Øian, E., Heimsund, B.-O., Eigestad, G.T., and Aavatsmark, I. 2006. Control volume discretisation on non-matching meshes in 3D. Paper B015 presented at the 10th European Conference on the Mathematics of Oil Recovery (ECMOR X), Amsterdam, 4–7 September.

Pal, M. and Edwards, M.G. 2007. Quasimonotonic Continuous Darcy-Flux Approximation for General 3D Grids of Any Element Type. Paper SPE 106486 presented at the SPE Reservoir Simulation Symposium, Houston, 26–28 February. doi: 10.2118/106486-MS.

Pal, M., Edwards, M.G., and Lamb, A.R. 2006. Convergence study of a family of flux-continuous, finite-volume schemes for the general tensor pressure equation. *Int. J. Numer. Methods Fluids* **51** (9): 1177–1203. doi: 10.1002/fld.1211.

Wheeler, M.F. and Yotov, I. 2006a. A cell-centered finite difference method on quadrilaterals. In *Compatible Spatial Discretizations*, ed. D.N. Arnold, P.B. Bochev, R.B. Lehoucq, R.A. Nicolaides, and M. Shashkov, Vol. 142, 189–207. New York: The IMA Volumes in Mathematics and its Applications, Springer.

Wheeler, M.F. and Yotov, I. 2006b. A multipoint flux mixed finite element method. *SIAM J. Numer. Anal.* **44** (5): 2082–2106. doi: 10.1137/050638473.

Wu, X.H. and Parashkevov, R.R. 2009. Effect of Grid Deviation on Flow Solutions. *SPE J.* **14** (1): 67–77. SPE-92868-PA. doi: 10.2118/92868-PA.

Ivar Aavatsmark is a principal researcher at the Centre for Integrated Petroleum Research and an adjoint professor in applied and computational mathematics at the University of Bergen, Norway. His research interests include mathematical modeling of flow in porous media and numerical methods for solving partial differential equations. He is an SPE member. **Geir Terje Eigestad** works as a senior reservoir engineer and is a partner and cofounder of Perecon AS consultancy company. He has been employed as acting associate professor at Department of Mathematics, University of Bergen. His professional interests are in advanced reservoir simulation for the petroleum industry, and his research background is in mathematical modeling of porous medium flow and discretization methods. **Bjørn-Ove Heimsund** is a specialist reservoir engineer with Total E&P Norge AS. He works with naturally fractured carbonate reservoirs and deeper exploration frontiers. **Brad Mallison** is a senior research scientist at Chevron Energy Technology Company in San Ramon, California. His research has been focused on mathematical and computational aspects of modeling flow and transport in porous media. **Jan Martin Nordbotten** is an Associate Professor at the Department of Mathematics, University of Bergen, Norway, and holds an appointment at the Department of Civil and Environmental Engineering at Princeton University. His research covers all aspects of numerical modeling and simulation of flow in porous media, with an emphasis on processes relevant for CO_2 storage. Nordbotten is the recipient of the inaugural Society of Industrial and Applied Mathematics Geosciences (SIAM-GS) Junior Scientist Award in 2009. He is a member of SPE. **Erlend Øian** works as a senior reservoir engineer and is a partner and cofounder of Perecon AS consultancy company. He is a former researcher at the Centre for Integrated Petroleum Research with research interest in computational methods and reservoir modeling. He is a member of SPE.